Supporting Information: Aerosol-Induced Closure of Marine Cloud Cells: Enhanced Effects in the Presence of Precipitation

Matthew W. Christensen[1], Peng Wu[1], Adam Varble[1], Heng Xiao[1], and Jerome Fast[1]

[1]Atmospheric Science & Global Change Division, Pacific Northwest National Laboratory, Richland, WA 99354, Washington, USA

Correspondence: Matthew Christensen (matt.christensen@pnnl.gov)

1 Contents of this file:

- Text S1 – S2
- Figure S1 – S15
- Table S1 – S10

2 Text S1

The European Centre for Medium-Range Weather Forecasts (ECMWF) ERA-5 product which provides spatially gridded meteorological profiles at 0.25-degree spatial resolution with 37 vertical pressure levels is provided once every hour (Hersbach et al., 2020). To test the sensitivity to boundary conditions, we have run WRF simulations comparing ERA5 to MERRA-2 boundary conditions. Figure S1 shows similar cloud water mixing ratios as well as its enhancement by increased aerosol concentration for both MERRA-2 and ERA5 at 13:00 UTC. The temperature profiles from WRF are also similar between reanalysis products. On average, the simulated cloud water mixing ratio values are larger when using MERRA-2 reanalysis, but the WRF simulations that use MERRA-2 also have a deeper PBL which allow for slightly higher clouds. Cloud property differences between the WRF simulations that use different reanalysis products are generally small relative to the differences between the aerosol experiments using the same meteorology. Therefore, the choice of using MERRA-2 or ERA5 reanalysis product at these scales does not significantly change the results.

3 Text S2

The derivation of the aerosol indirect radiative effect follows from the methodology described in Quaas et al. (2008b) and Christensen et al. (2023). The derivation follows from the change in reflected solar radiation caused by a change in the planetary albedo and N_d and can be written as

$$RE_{aci} = \overline{F^{\downarrow}} \frac{d\alpha}{dN_d} \overline{\Delta N_d} \tag{1}$$

where, $\overline{F^{\downarrow}}$ is the mean top of atmosphere (TOA) incoming solar radiation, α is the planetary albedo, and N_d is the droplet concentration. α can be expanded into contributions from the surface and clouds following

$$\alpha = (1 - f_c)\alpha_{sfc}\phi_{atm} + \alpha_c \phi_{atm} f_c \tag{2}$$

where ϕ_{atm} is the transfer function that accounts for the average albedo of the non-cloudy air above the surface and takes an average value of 0.7 (Diamond et al., 2020). α_c can be estimated using the two-stream delta Eddington approximation as $\alpha_c = \frac{(1-g)\tau_c}{2+(1-g)\tau_c}$ where, g is the asymmetry parameter and takes a value of 0.85 for liquid clouds and τ_c is the cloud optical thickness. τ_c is approximated using an adiabatic assumption as $\tau_c = \gamma' L^{\frac{5}{6}} N_d^{\frac{1}{3}}$ where $\gamma' \approx 0.185\,\mathrm{kg}^{-5/6}\mathrm{m}^{8/3}$ and L is the LWP which is approximated as $L = (2/3)\rho_w r_e \tau_c$ (Stephens, 1978) with the density of water, ρ_w, cloud droplet effective radius, r_e, and the cloud droplet concentration, N_d.

We use the equivalent form of $N_d = \gamma\sqrt{\tau_c} r_e^{-2.5}$, where $\gamma = 1.37 \times 10^{-5}\mathrm{m}^{-0.5}$ to compute cloud droplet number concentration from cloud effective radius and optical depth variables following Grosvenor et al. (2018). Following similar approaches to (Quaas et al., 2008a) and (Christensen et al., 2022), taking the derivative of α with respect to N_d gives

$$\frac{d\alpha}{dN_d} = \phi_{atm}\left(-\alpha_{sfc}\frac{\partial f_c}{\partial N_d} + \alpha_c \frac{\partial f_c}{\partial N_d} + f_c \frac{\partial \alpha_c}{\partial N_d}\right) \tag{3}$$

where cloud-free conditions give $\frac{\partial \alpha_{sfc}}{\partial N_d} = 0$. The chain rule expansion of $\frac{d\alpha_c}{dN_d} = \frac{\partial \tau_c}{\partial N_d}\frac{\partial \alpha_c}{\partial \tau_c}$ can be solved by the following two derivatives: 1) $\frac{\partial \tau_c}{\partial N_d} = \frac{\tau_c}{3N_d}\left(1 + \frac{5}{2}\frac{\partial \ln N_d}{\partial \ln L}\right)$ and 2) $\frac{\partial \alpha_c}{\partial \tau_c} = \frac{\alpha_c(1-\alpha_c)}{\tau_c}$. Combining with equation (3) gives the resulting equation

$$RE_{aci} = -\overline{F^{\downarrow}}\phi_{atm}\overline{\frac{f_c\alpha_c(1-\alpha_c)}{3N_d}}\left(1 + \frac{5}{2}\frac{\Delta \ln L}{\Delta \ln N_d} + \overline{\frac{3(\alpha_c - \alpha_{sfc})}{\alpha_c(1-\alpha_c)}}\frac{\Delta \ln f_c}{\Delta \ln N_d}\right)\overline{\Delta N_d} \tag{4}$$

which is used to compute the aerosol indirect shortwave radiative effect. The Δ symbols denote differences between aerosol experiments of varying aerosol concentrations. The $\overline{\frac{f_c\alpha_c(1-\alpha_c)}{3N_d}}$ and $\overline{\frac{3(\alpha_c-\alpha_{sfc})}{\alpha_c(1-\alpha_c)}}$ are computed from the average of two paired aerosol experiments and $\overline{N_d}$ represents the difference between two paired aerosol experiments. The three terms inside the parentheses are regarded in order as the Twomey effect, liquid water path adjustment, and cloud fraction adjustment.

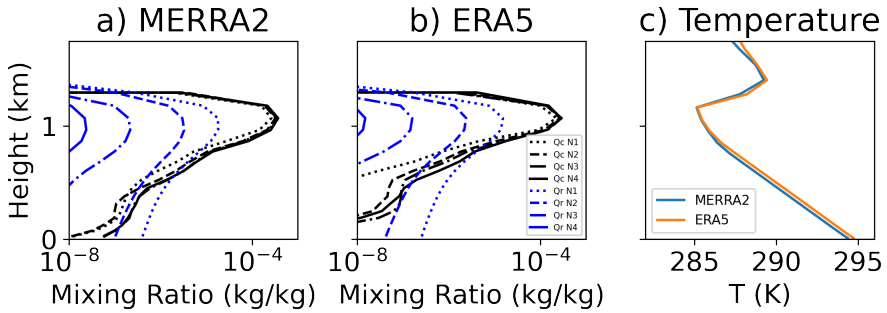

Figure S1. Vertical profile of the cloud water mixing ratio on 07/18/2017 averaged over an hour from 13:00 UTC simulated for pristine (N1; dotted), clean (N2; dashed), control (N3; dotted-dashed), and polluted (N4; solid) experiments using a) MERRA2 and b) ERA5 reanalysis meteorology for the boundary conditions. Air temperature is from WRF using MERRA2 and ERA5 are displayed in (c).

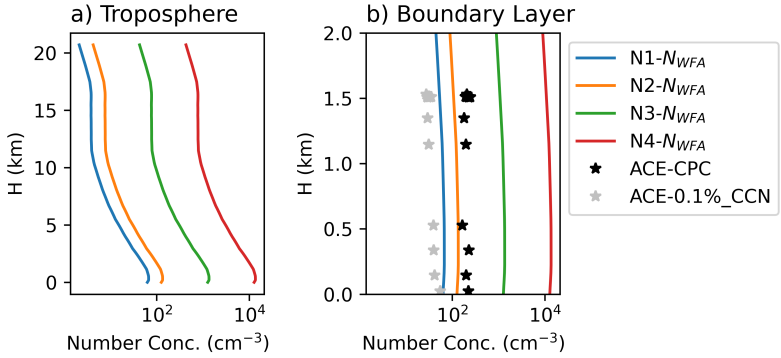

Figure S2. Vertical profile of the background number of water friendly aerosol (NWFA) concentrations for pristine (N1), clean (N2), control (N3), and polluted (N4) conditions on 7/18/17 at 13:00 UTC using the Thompson (aerosol-aware) scheme plotted over the a) whole troposphere and b) boundary layer with observations of the total condensation particle counter (CPC; black asterisks) and CCN at 0.2% supersaturation (gray asterisks) from aircraft measurements taken between 10:00 – 16:00 UTC. Note, aerosol data is omitted when total cloud water content as measured by the aircraft in the WCM-2000 data set

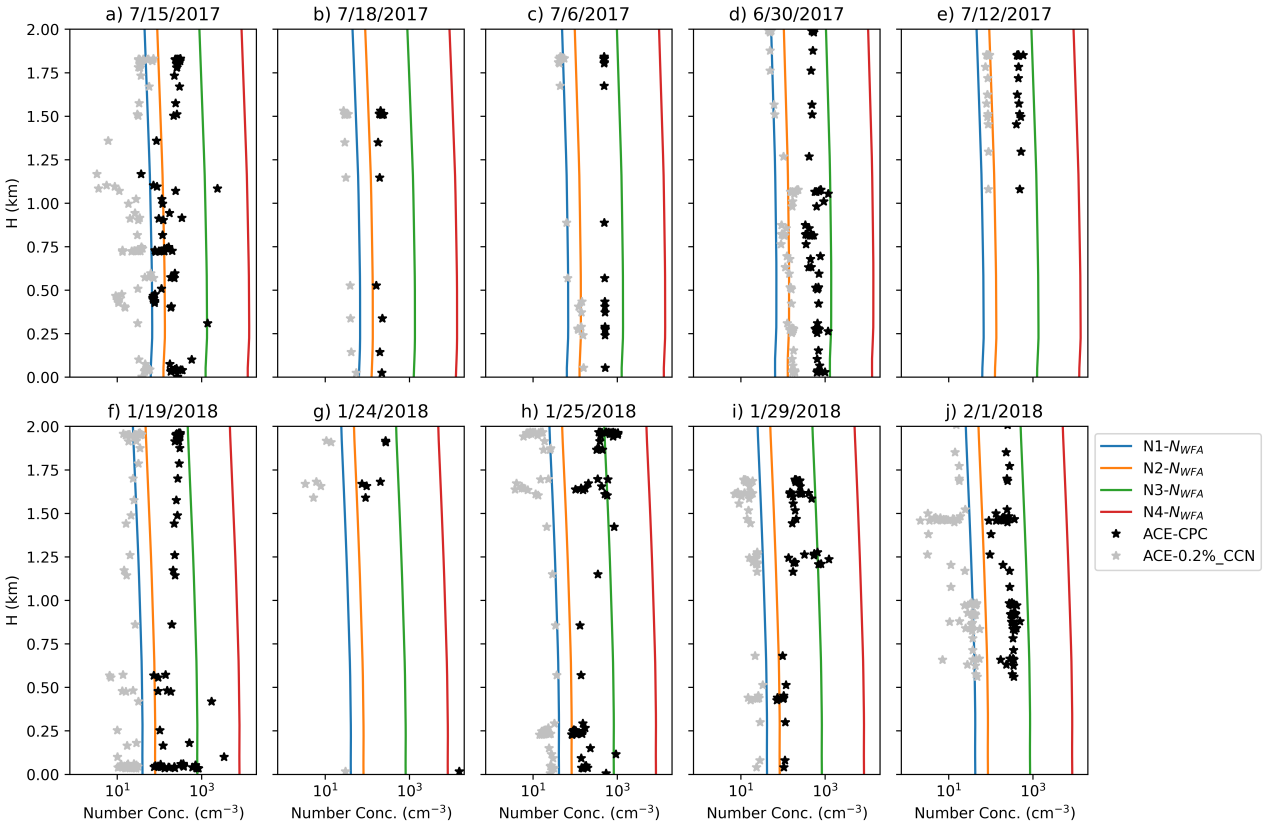

Figure S3. Same as Figure S2b except showing all of the case study experiments.

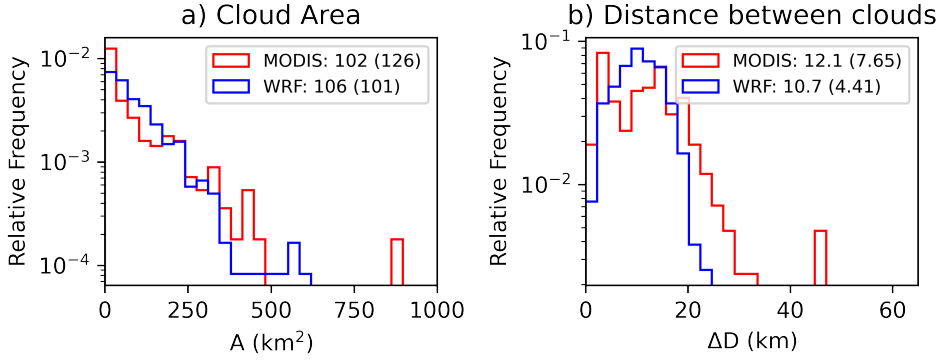

Figure S4. Histogram of the (a) areal extent and (b) minimum distance between cell centroids detected using the watershed algorithm for the 7/18/17 case study at 13:00 UTC. Means and standard deviations (shown in parenthesis) are shown for both MODIS (red) and WRF (blue) data sets.

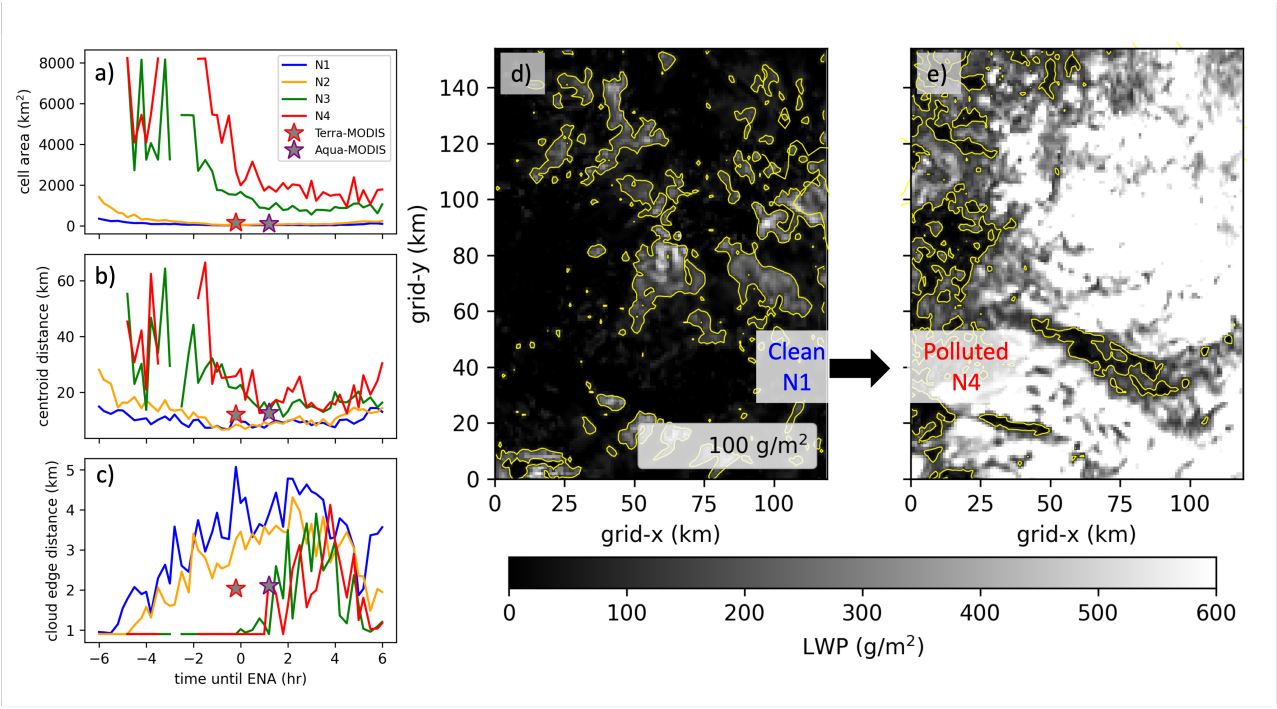

Figure S5. Time-series of the average (a) cloud object area, (b) minimum distance between cloud centroids, (c) minimum distance between cloud edges over each 15-minute time-interval detected for pristine (blue), clean (orange), control (green), and polluted (red) experiments on 07/15/2017. MODIS averages (star) and standard deviations (vertical lines) are displayed on the image. LWP at 13 UTC is displayed for the clean (d) and polluted experiments (e).

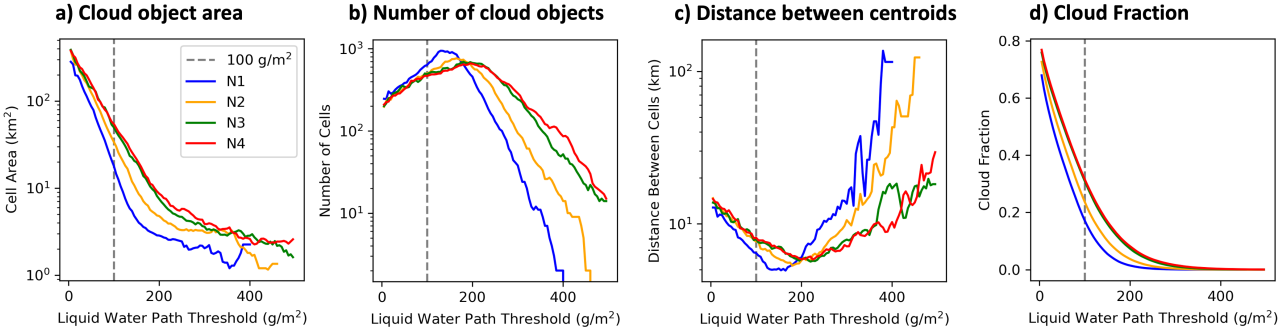

Figure S6. Cloud object area (a), number of clouds over the inner domain (b), and distance between clouds (c) as a function of the LWP threshold used to determine the cloud object boundaries for pristine (blue), clean (orange), control (green), and polluted (red) WRF simulations. The dashed line represents the 100 g m^{-2} threshold used throughout the study.

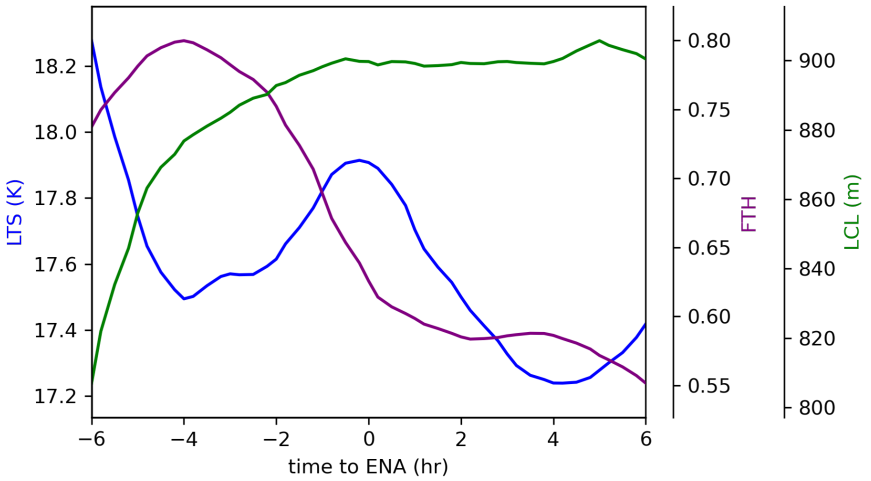

Figure S7. Lower tropospheric stability (i.e. the difference in potential temperature between the surface and 700 hPa; blue), free tropospheric humidity (relative humidity at 850 hPa; purple), and lifted condensation level (purple) computed using MERRA-2 thermodynamic profiles along the 07/18/2017 trajectory case study.

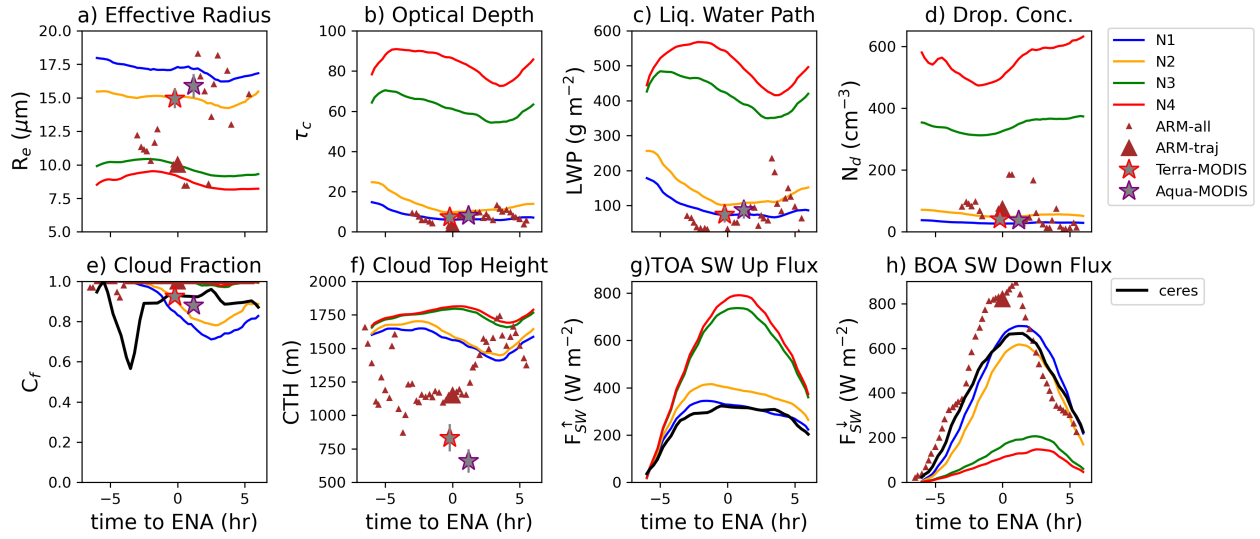

Figure S8. a) Droplet effective radius (R_e), b) cloud optical thickness (τ_c) retrieved from the 3.7-μm band, c) liquid water path (LWP), d) droplet concentration (N_d) computed from R_e and τ_c, e) liquid cloud fraction (C_f), f) cloud top height (CTH), g) top of atmosphere outgoing shortwave radiative flux ($F^{\uparrow}_{SW}$, and h) bottom of atmosphere incoming shortwave flux ($F^{\downarrow}_{SW}$ for pristine (blue), clean (orange), control (green), and polluted (red) WRF simulations. WRF-Solar was used for comparison with the satellite retrievals. ARM (brown diamond) retrievals are provided at all time steps and at the time when the trajectory passes over the ARM site (larger brown diamond) and MODIS retrievals from satellites Terra (red star) and Aqua (blue star) are provided when available along the trajectory on 07/15/2017. Hourly retrievals of the cloud fraction and radiative fluxes are provided by CERES. Note, aside from time to ENA equals 0, the ARM measurements do not coincide with the trajectory location and are merely used to show Eulerian variability.

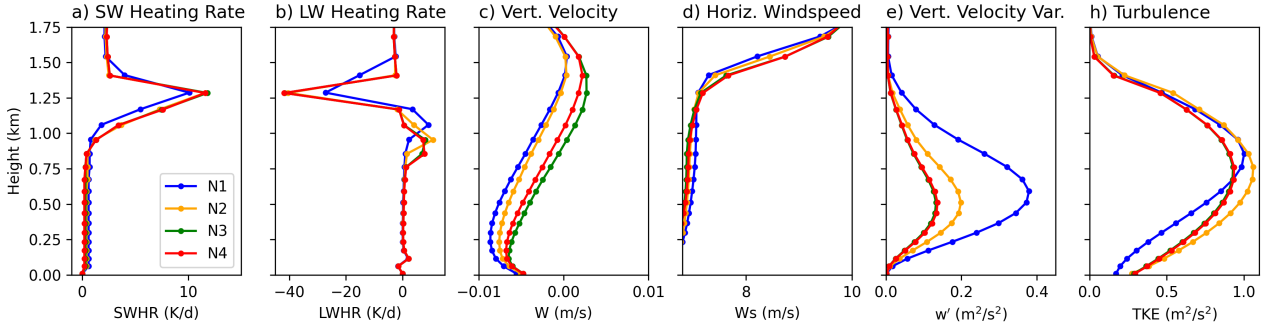

Figure S9. Vertical profile of the a) mean shortwave and b) longwave radiative heating rate, c) mean vertical velocity, d) mean horizontal wind speed, e) vertical velocity variance, and h) turbulent kinetic energy (TKE) for pristine (blue), unpolluted (orange), control (green), and polluted (red) WRF simulations on 07/18/2017 at 13:00 UTC.

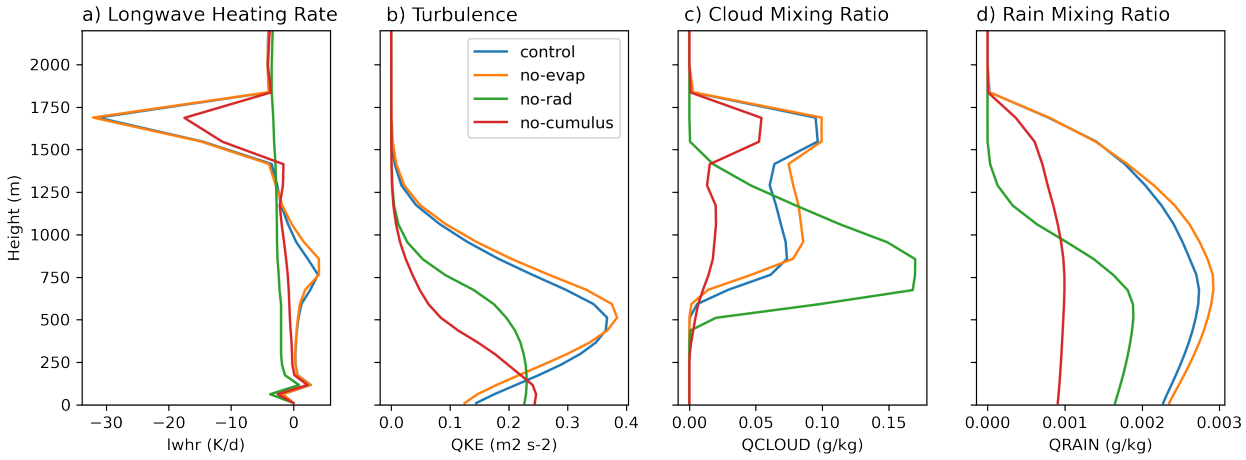

Figure S10. Vertical profiles at 13:00 UTC on the case study day (07/15/2017) for a) longwave radiative cooling rate, b) turbulent kinetic energy, c) cloud water mixing ratio, and d) rainwater mixing ratio. Results are shown for the control experiment, as well as experiments with no evaporative cooling from cloud and raindrops, no radiation to the cloud layer, and with the cumulus scheme turned off in the WRF model.

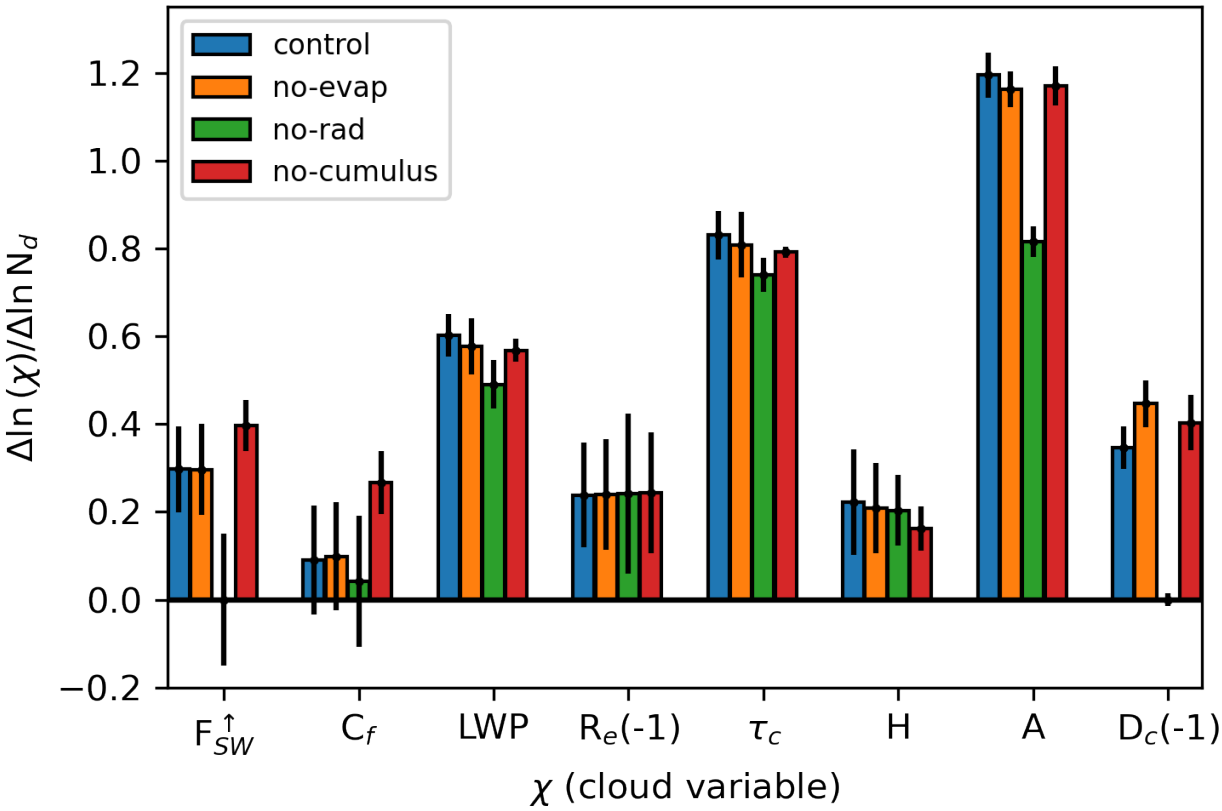

Figure S11. Values of the slope in the log change of a given variable (χ) to the log change in cloud droplet number concentration (N_d), computed from two aerosol WRF experiment simulations. The results are presented for the control experiment, as well as experiments with no evaporative cooling from cloud and raindrops, no radiation to the cloud layer, and with the cumulus scheme turned off in the WRF model, all for the case study day on 07/15/2017 at 13:00 UTC. The χ variables include top-of-atmosphere outgoing shortwave flux ($F^{\uparrow}_{SW}$), liquid cloud fraction (C_f), liquid water path (LWP), effective droplet radius (R_e), cloud optical thickness (τ_c), cloud thickness (H), cloud object area (A), and distance bewtween cloud object centroids (D_c).

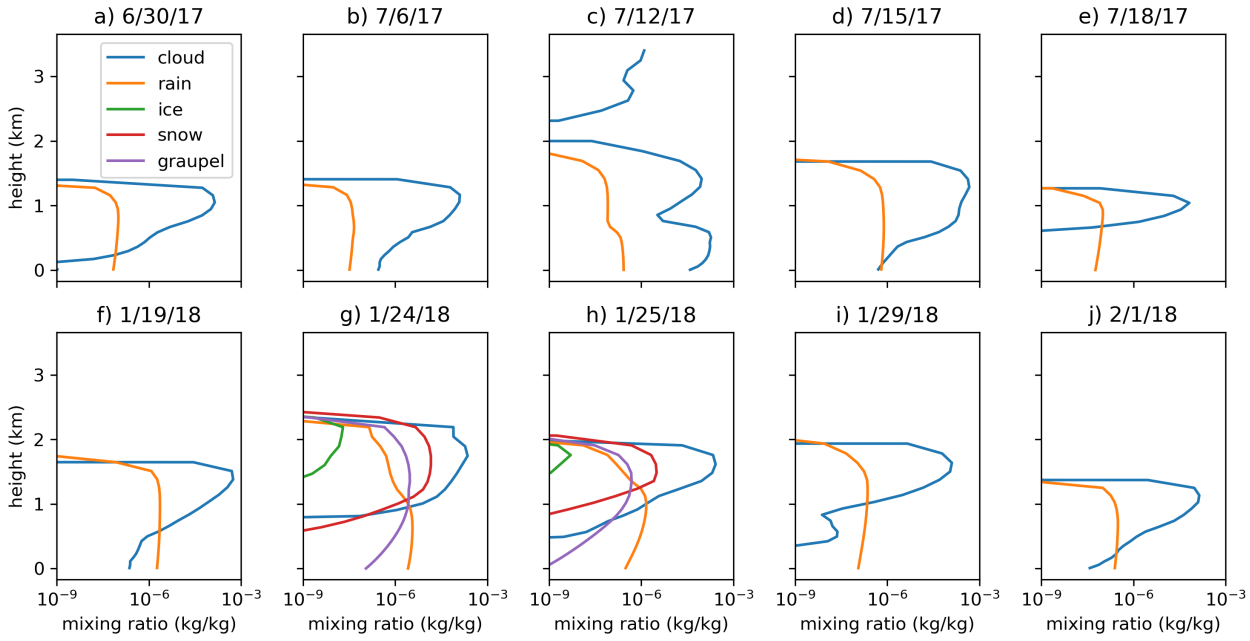

Figure S12. Vertical profile of the cloud, rain, ice, snow, and graupel mixing ratios for each case study at 13:00 UTC simulated for the control aerosol experiment using MERRA-2 reanalysis metoerology for the boundary condition.

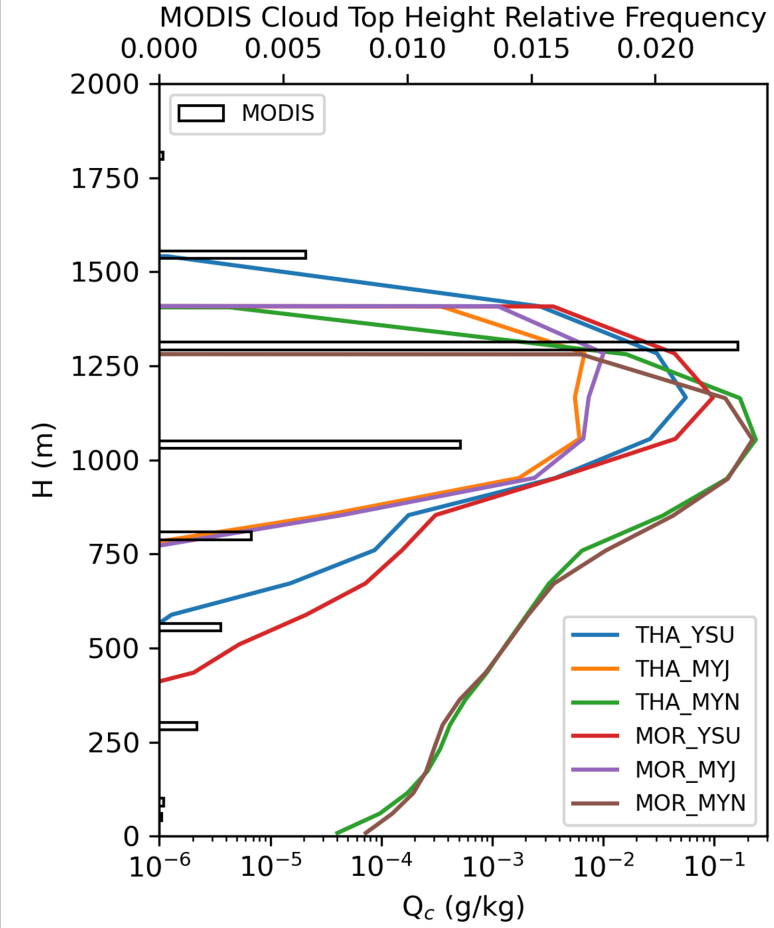

Figure S13. Vertical profile of cloud water mixing ratio (Q_c) from each of the microphysics and PBL scheme combinations described in Table 2. Normalized histogram of MODIS cloud top height retrievals (black rectangles) are plotted on a separate x-axis.

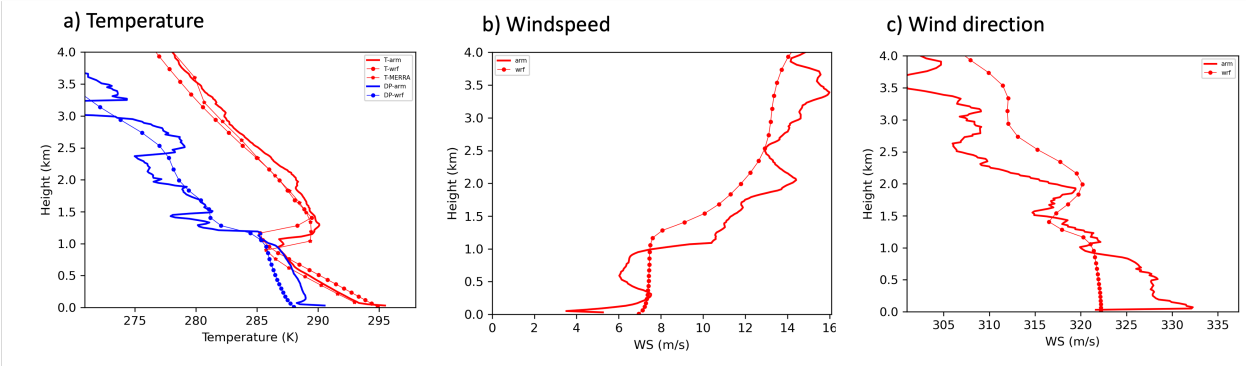

Figure S14. a) Vertical profile of air temperature (red) and dew point temperature (blue) from interpolated sonde measurements at the arm site at Graciosa Island (solid), as well as the simulations from WRF (solid with circles) and raw MERRA2 data, b) wind speed, and c) wind direction from ARM measurements and WRF simulations on 7/18/2017 at 13:00 UTC.

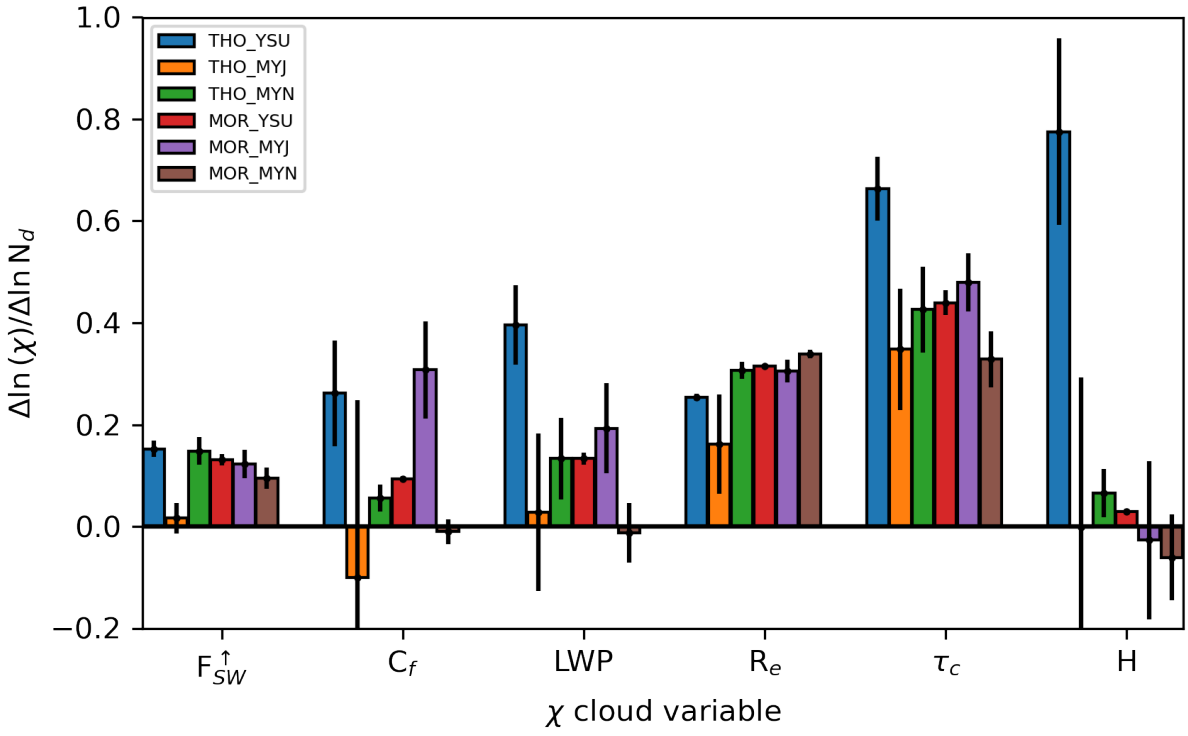

Figure S15. Value of the slope in the log change of a given variable (χ) to the log change in cloud droplet number concentration (N_d) computed from 4 aerosol WRF experiments simulations on 7/18 represented at 13:00 UTC for 6 different WRF configurations; 3 PBL schemes (YSU, MYJ, MYN) and 2 microphysics schemes (Thompson and Morrison). χ variables shown are: top of atmosphere outgoing shortwave flux ($F^{\uparrow}_{SW}$), liquid cloud fraction (C_f), liquid water path (LWP), effective droplet radius (R_e), cloud optial thickness (τ_c), and cloud thickness (H)

Table S1. Case study day 7/15/17 (with daily-mean solar insolation, $\overline{F^{\downarrow}}$ =485.0 W m^{-2}) WRF simulated cloud properties for each experiment (N1, N2, N3, N4; corresponding to pristine, clean, control, and polluted) on each case study day. Radiative effects are computed using 6 different combinations of the experiments. Averages and standard deviations of all experiments are provided.

Quantity	N1	N2	N3	N4			
N_d (cm^{-3})	30.1	55.7	365	599			
LWP (g m^{-2})	73.9	120	361	432			
f_c	0.77	0.84	0.99	0.99			
α_{cld}	0.32	0.47	0.81	0.85			
	Δ(N4-N3)	Δ(N4-N2)	Δ(N4-N1)	Δ(N3-N2)	Δ(N3-N1)	Δ(N2-N1)	exp. mean
Twomey effect (W m^{-2})	-7.72	-38.55	-43.59	-35.06	-41.32	-12.92	-29.86 $\pm$ 14.1
LWP adjustment (W m^{-2})	-7.02	-51.84	-64.37	-51.14	-65.67	-25.69	-44.29 $\pm$ 21.2
C$_f$ adjustment (W m^{-2})	-0.81	-20.19	-22.28	-21.26	-23.58	-6.82	-15.82 $\pm$ 8.73

Table S2. Same as Table S1 except for case study day 7/18/17 (with daily-mean solar insolation, $\overline{F^{\downarrow}}$ =481.8 W m^{-2}).

Quantity	N1	N2	N3	N4			
N_d (cm^{-3})	49.8	78.0	293	463			
LWP (g m^{-2})	94.3	120	136	138			
f_c	0.90	0.92	0.92	0.92			
α_{cld}	0.40	0.49	0.63	0.67			
	Δ(N4-N3)	Δ(N4-N2)	Δ(N4-N1)	Δ(N3-N2)	Δ(N3-N1)	Δ(N2-N1)	exp. mean
Twomey effect (W m^{-2})	-10.56	-35.93	-41.17	-29.56	-36.36	-11.17	-27.46 $\pm$ 12.2
LWP adjustment (W m^{-2})	-0.75	-7.12	-17.83	-7.15	-19.12	-15.25	-11.20 $\pm$ 6.65
C$_f$ adjustment (W m^{-2})	-0.48	-0.58	-2.32	-0.25	-2.17	-2.01	-1.30 $\pm$ 0.87

Table S3. Same as Table S1 except for case study day 7/6/17 (with daily-mean solar insolation, $\overline{F^{\downarrow}}$ =492.7 W m^{-2}).

Quantity	N1	N2	N3	N4			
N_d (cm^{-3})	32.4	58.5	203	395			
LWP (g m^{-2})	39.4	38.8	46.2	42.8			
f_c	0.14	0.15	0.23	0.23			
α_{cld}	0.23	0.29	0.41	0.42			
	Δ(N4-N3)	Δ(N4-N2)	Δ(N4-N1)	Δ(N3-N2)	Δ(N3-N1)	Δ(N2-N1)	exp. mean
Twomey effect (W m^{-2})	-4.09	-7.42	-8.09	-5.43	-6.76	-1.86	-5.61 $\pm$ 2.13
LWP adjustment (W m^{-2})	1.15	-0.97	-0.67	-1.90	-1.44	0.14	-0.61 $\pm$ 1.01
C$_f$ adjustment (W m^{-2})	-0.43	-5.81	-4.73	-6.11	-5.06	-0.19	-3.72 $\pm$ 2.46

Table S4. Same as Table S1 except for case study day 6/30/17 (with daily-mean solar insolation, $\overline{F^{\downarrow}}$ =496.0 W m^{-2}).

Quantity	N1	N2	N3	N4			
N_d (cm^{-3})	32.2	56.8	223	407			
LWP (g m^{-2})	44.2	51.2	53.1	52.4			
f_c	0.43	0.47	0.50	0.52			
α_{cld}	0.24	0.31	0.42	0.46			
	Δ(N4-N3)	Δ(N4-N2)	Δ(N4-N1)	Δ(N3-N2)	Δ(N3-N1)	Δ(N2-N1)	exp. mean
Twomey effect (W m^{-2})	-8.54	-20.38	-21.26	-15.42	-17.80	-5.69	-14.85 $\pm$ 5.84
LWP adjustment (W m^{-2})	0.43	-0.61	-3.59	-1.01	-4.22	-3.69	-2.11 $\pm$ 1.78
C$_f$ adjustment (W m^{-2})	-1.91	-4.05	-5.58	-2.94	-4.87	-2.44	-3.63 $\pm$ 1.31

Table S5. Same as Table S1 except for case study day 7/12/17 (with daily-mean solar insolation, $\overline{F^{\downarrow}}$ =487.9 W m^{-2}).

Quantity	N1	N2	N3	N4			
N_d (cm^{-3})	35.3	58.4	281	586			
LWP (g m^{-2})	71.4	84.9	120	120			
f_c	0.64	0.66	0.71	0.72			
α_{cld}	0.33	0.39	0.60	0.65			
	Δ(N4-N3)	Δ(N4-N2)	Δ(N4-N1)	Δ(N3-N2)	Δ(N3-N1)	Δ(N2-N1)	exp. mean
Twomey effect (W m^{-2})	-13.51	-32.16	-34.50	-25.61	-29.87	-8.40	-24.01 $\pm$ 9.72
LWP adjustment (W m^{-2})	-0.11	-12.27	-16.11	-14.24	-18.80	-7.22	-11.46 $\pm$ 6.20
C$_f$ adjustment (W m^{-2})	-1.86	-6.80	-6.81	-6.29	-6.53	-1.20	-4.91 $\pm$ 2.41

Table S6. Same as Table S1 except for case study day 1/19/18 (with daily-mean solar insolation, $\overline{F^{\downarrow}}$ =178.4 W m^{-2}).

Quantity	N1	N2	N3	N4			
N_d (cm^{-3})	25.3	28.2	211	541			
LWP (g m^{-2})	47.9	46.0	191	315			
f_c	0.62	0.65	0.87	0.92			
α_{cld}	0.24	0.24	0.67	0.81			
	Δ(N4-N3)	Δ(N4-N2)	Δ(N4-N1)	Δ(N3-N2)	Δ(N3-N1)	Δ(N2-N1)	exp. mean
Twomey effect (W m^{-2})	-6.26	-14.63	-14.52	-12.01	-12.12	-0.53	-10.01 $\pm$ 5.07
LWP adjustment (W m^{-2})	-8.36	-23.87	-22.35	-21.25	-19.74	0.49	-15.85 $\pm$ 8.89
C$_f$ adjustment (W m^{-2})	-3.25	-8.85	-9.57	-7.73	-8.53	-0.50	-6.41 $\pm$ 3.34

Table S7. Same as Table S1 except for case study day 1/24/18 (with daily-mean solar insolation, $\overline{F^{\downarrow}}$ =198.1 W m^{-2}).

Quantity	N1	N2	N3	N4			
N_d (cm^{-3})	165	172	244	453			
LWP (g m^{-2})	225	230	251	257			
f_c	0.96	0.96	0.96	0.96			
α_{cld}	0.68	0.69	0.73	0.77			
	Δ(N4-N3)	Δ(N4-N2)	Δ(N4-N1)	Δ(N3-N2)	Δ(N3-N1)	Δ(N2-N1)	exp. mean
Twomey effect (W m^{-2})	-5.00	-7.86	-8.20	-3.15	-3.52	-0.37	-4.68 $\pm$ 2.73
LWP adjustment (W m^{-2})	-0.50	-2.21	-2.71	-1.91	-2.47	-0.58	-1.73 $\pm$ 0.88
C$_f$ adjustment (W m^{-2})	-0.30	-0.10	-0.17	0.19	0.11	-0.07	-0.06 $\pm$ 0.17

Table S8. Same as Table S1 except for case study day 1/25/18 (with daily-mean solar insolation, $\overline{F^{\downarrow}}$ =194.7 W m^{-2}).

Quantity	N1	N2	N3	N4			
N_d (cm^{-3})	13.8	21.6	147	319			
LWP (g m^{-2})	21.8	22.2	46.2	50.3			
f_c	0.001	0.01	0.64	0.67			
α_{cld}	0.11	0.12	0.37	0.43			
	Δ(N4-N3)	Δ(N4-N2)	Δ(N4-N1)	Δ(N3-N2)	Δ(N3-N1)	Δ(N2-N1)	exp. mean
Twomey effect (W m^{-2})	-5.26	-5.43	-5.50	-4.10	-4.38	-0.01	-4.11 $\pm$ 1.91
LWP adjustment (W m^{-2})	-1.43	-4.12	-3.64	-3.92	-3.46	-0.001	-2.76 $\pm$ 1.52
C$_f$ adjustment (W m^{-2})	-1.03	-21.35	-28.10	-19.79	-25.89	-0.03	-16.03 $\pm$ 11.3

Table S9. Same as Table S1 except for case study day 1/29/18 (with daily-mean solar insolation, $\overline{F^{\downarrow}}$ =200.1 W m^{-2}).

Quantity	N1	N2	N3	N4			
N_d (cm^{-3})	21.8	35.9	226	484			
LWP (g m^{-2})	14.3	32.7	110	103			
f_c	0.15	0.47	0.78	0.79			
α_{cld}	0.14	0.21	0.57	0.62			
	Δ(N4-N3)	Δ(N4-N2)	Δ(N4-N1)	Δ(N3-N2)	Δ(N3-N1)	Δ(N2-N1)	exp. mean
Twomey effect (W m^{-2})	-6.39	-12.29	-9.38	-10.08	-8.14	-1.02	-7.88 $\pm$ 3.56
LWP adjustment (W m^{-2})	1.44	-13.57	-14.98	-16.68	-17.85	-4.25	-10.98 $\pm$ 7.09
C$_f$ adjustment (W m^{-2})	-0.50	-9.45	-18.02	-10.08	-19.29	-3.72	-10.18 $\pm$ 6.84

Table S10. Same as Table S1 except for case study day 2/1/18 (with daily-mean solar insolation, $\overline{F^{\downarrow}}$ =208.6 W m^{-2}).

Quantity	N1	N2	N3	N4			
N_d (cm^{-3})	18.3	32.1	198	410			
LWP (g m^{-2})	39.3	53.4	78.8	81.9			
f_c	0.44	0.48	0.66	0.71			
α_{cld}	0.19	0.27	0.49	0.55			
	Δ(N4-N3)	Δ(N4-N2)	Δ(N4-N1)	Δ(N3-N2)	Δ(N3-N1)	Δ(N2-N1)	exp. mean
Twomey effect (W m^{-2})	-5.78	-11.91	-11.94	-9.41	-10.01	-2.16	-8.54 $\pm$ 3.52
LWP adjustment (W m^{-2})	-0.78	-5.00	-7.05	-5.02	-7.30	-2.94	-4.68 $\pm$ 2.27
C$_f$ adjustment (W m^{-2})	-2.53	-7.06	-6.21	-6.03	-5.38	-0.60	-4.64 $\pm$ 2.29

References

Christensen, M. W., Gettelman, A., Cermak, J., Dagan, G., Diamond, M., Douglas, A., Feingold, G., Glassmeier, F., Goren, T., Grosvenor, D. P., Gryspeerdt, E., Kahn, R., Li, Z., Ma, P.-L., Malavelle, F., McCoy, I. L., McCoy, D. T., McFarquhar, G., Mülmenstädt, J., Pal, S., Possner, A., Povey, A., Quaas, J., Rosenfeld, D., Schmidt, A., Schrödner, R., Sorooshian, A., Stier, P., Toll, V., Watson-Parris, D., Wood, R., Yang, M., and Yuan, T.: Opportunistic experiments to constrain aerosol effective radiative forcing, Atmospheric Chemistry and Physics, 22, 641–674, https://doi.org/10.5194/acp-22-641-2022, 2022.

Christensen, M. W., Ma, P.-L., Wu, P., Varble, A. C., Mülmenstädt, J., and Fast, J. D.: Evaluation of aerosol–cloud interactions in E3SM using a Lagrangian framework, Atmospheric Chemistry and Physics, 23, 2789–2812, https://doi.org/10.5194/acp-23-2789-2023, 2023.

Diamond, M. S., Director, H. M., Eastman, R., Possner, A., and Wood, R.: Substantial Cloud Brightening From Shipping in Subtropical Low Clouds, AGU Advances, 1, e2019AV000 111, https://doi.org/10.1029/2019AV000111, 2020.

Grosvenor, D. P., Sourdeval, O., Zuidema, P., Ackerman, A., Alexandrov, M. D., Bennartz, R., Boers, R., Cairns, B., Chiu, J. C., Christensen, M., Deneke, H., Diamond, M., Feingold, G., Fridlind, A., Hunerbein, A., Knist, C., Kollias, P., Marshak, A., McCoy, D., Merk, D., Painemal, D., Rausch, J., Rosenfeld, D., Russchenberg, H., Seifert, P., Sinclair, K., Stier, P., van Diedenhoven, B., Wendisch, M., Werner, F., Wood, R., Zhang, Z., and Quaas, J.: Remote Sensing of Droplet Number Concentration in Warm Clouds: A Review of the Current State of Knowledge and Perspectives, Reviews of Geophysics, 56, 409–453, https://doi.org/10.1029/2017RG000593, 2018.

Hersbach, H., Bell, B., Berrisford, P., Hirahara, S., Horányi, A., Muñoz-Sabater, J., Nicolas, J., Peubey, C., Radu, R., Schepers, D., Simmons, A., Soci, C., Abdalla, S., Abellan, X., Balsamo, G., Bechtold, P., Biavati, G., Bidlot, J., Bonavita, M., De Chiara, G., Dahlgren, P., Dee, D., Diamantakis, M., Dragani, R., Flemming, J., Forbes, R., Fuentes, M., Geer, A., Haimberger, L., Healy, S., Hogan, R. J., Hólm, E., Janisková, M., Keeley, S., Laloyaux, P., Lopez, P., Lupu, C., Radnoti, G., de Rosnay, P., Rozum, I., Vamborg, F., Villaume, S., and Thépaut, J.-N.: The ERA5 global reanalysis, Quarterly Journal of the Royal Meteorological Society, 146, 1999–2049, https://doi.org/https://doi.org/10.1002/qj.3803, 2020.

Quaas, J., Boucher, O., Bellouin, N., and Kinne, S.: Satellite-based estimate of the direct and indirect aerosol climate forcing, Journal of Geophysical Research: Atmospheres, 113, https://doi.org/10.1029/2007JD008962, 2008a.

Quaas, J., Boucher, O., Bellouin, N., and Kinne, S.: Satellite-Based Estimate of the Direct and Indirect Aerosol Climate Forcing, Journal of Geophysical Research: Atmospheres, 113, D05 204, https://doi.org/10.1029/2007jd008962, 2008b.

Stephens, G. L.: Radiation profiles in extended water clouds. II: Parameterization schemes, Journal of the Atmospheric Sciences, 35, 2123–2132, 1978.